



Effect of hydrogen on tensile properties and fracture behavior of PH 13-8 Mo steel

Xinfeng Li ^a, Jin Zhang ^b, Yanfei Wang ^c, Sicong Shen ^a, Xiaolong Song ^{a,*}

^a State Key Laboratory for Mechanical Behavior of Materials, School of Materials Science and Engineering, Xi'an Jiaotong University, Xi'an 710049, China

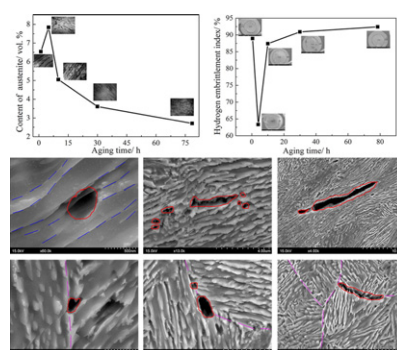
^b Department of Geosciences, Center for Materials by Design, State University of New York, Stony Brook, NY 11794-2100, USA

^c School of Chemical Engineering & Technology, China University of Mining and Technology, Xuzhou 221116, China

HIGHLIGHTS

- Hydrogen slightly increases yield strength and decreases tensile strength.
- The susceptibility to hydrogen embrittlement is the lowest in the specimen aged for 4 h.
- Hydrogen-induced cracks initiate from lath, packet and grain boundaries.
- Hydrogen-induced crack propagation passes through lath boundaries and walks along packet, grain boundaries.

GRAPHICAL ABSTRACT



ARTICLE INFO

Article history:

Received 5 April 2016

Received in revised form 24 June 2016

Accepted 27 June 2016

Available online 29 June 2016

Keywords:

Hydrogen embrittlement

PH 13-8 Mo steel

Aging time

Fracture behavior

ABSTRACT

The tensile properties and fracture behavior of PH 13-8 Mo steel after subjected to pre-charged hydrogen were investigated by slow strain rate tensile tests. The results suggest that hydrogen slightly increases yield strength, while decreases tensile strength. The susceptibility to hydrogen embrittlement of specimens aged at 650 °C firstly reduces and then increases as the aging time increases, reaching the lowest value at aging time 4 h. This is dominantly attributed to the highest content of austenite. Moreover, hydrogen-induced crack nucleation sites initiate from lath, packet and prior austenite grain boundaries. Crack propagation passes through lath boundaries and walks along packet, prior austenite grain boundaries. Scanning electron microscopy result indicates that hydrogen-charged specimens show quasi-cleavage fracture and intergranular fracture in annular brittle zone while dimple fracture is observed in hydrogen-free specimens.

© 2016 Elsevier Ltd. All rights reserved.

1. Introduction

PH 13-8 Mo, a precipitation-hardening martensitic stainless steel, has combined high strength with good levels of resistance to both general corrosion and stress-corrosion cracking. The alloy has also exhibited good ductility and toughness in both the longitudinal and transverse

directions. Thus it has been widely used in machinery fields and aircraft applications, such as nuclear reactor components and landing gear parts [1,2]. On the one hand, the nanometer-sized NiAl precipitates take place in PH 13-8 Mo steel during aging treatment. These precipitates exhibit an ordered B2 structure and are responsible for its high strength. In addition, these fine NiAl precipitates are found to maintain coherency with the matrix even when over-aged at 620 °C for 4 h [3,4]. On the other hand, the reversion from martensite to austenite can occur and the amount of reverted austenite depends on aging temperature [5–7] as

* Corresponding author.

E-mail address: songxl@mail.xjtu.edu.cn (X. Song).

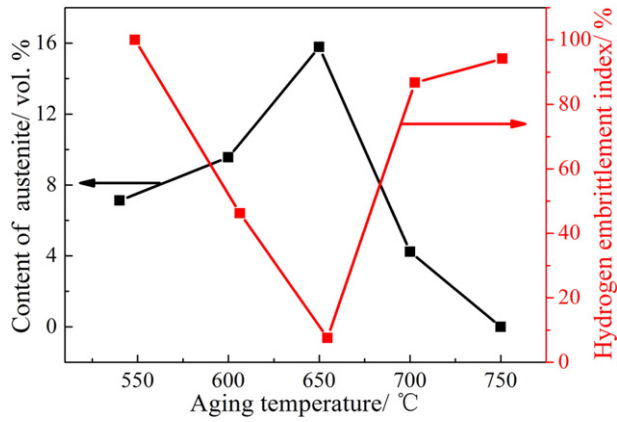


Fig. 1. Effect of aging temperature on content of austenite and hydrogen embrittlement index of PH 13-8 Mo steel [7].

Table 1

Chemical composition of the steel (mass%).

Element	C	Si	Mn	Cr	Ni	Mo	Al	N	Fe
	0.03	0.05	0.10	12.50	8.00	2.30	1.1	0.003	Balance

well as on aging time [1,8]. Blime et al. [6] reported that the ductility and toughness increased while the strength and hardness decreased with increasing aging temperature in the cast PH 13-8 Mo steel. Schnitzer et al. [1] found that the volume fraction of reverted austenite increased from 7% to 30% when aging time varied from 3 h to 100 h.

The influence of hydrogen on mechanical properties of PH 13-8 Mo steel has been investigated. Ding et al. [9] indicated that as compared with the counterpart specimens tested in air, hydrogen accelerated the fatigue crack growth rates. Yong et al. [10] reported that PH 13-8 Mo steel was severely embrittled by hydrogen and the value of fracture toughness was degraded up to 98% in the presence of hydrogen. The fracture mode exhibited transgranular microvoid coalescence for uncharged specimen while hydrogen-charged specimen failed by intergranular cracking or transgranular cleavage fracture. Moreover, Tsay et al. [11,12] investigated hydrogen-induced crack of PH 13-8 Mo steel, indicating that over-aged (H1100) specimen showed higher resistance to hydrogen embrittlement and lower hydrogen diffusivity behavior due to the formation of reverted austenite.

Our previous study [7] has investigated the effect of tensile rate and aging temperature on hydrogen embrittlement sensibility of PH 13-8 Mo steel, revealing that the sample aged at 650 °C exhibits the highest resistance to hydrogen embrittlement, which is ascribed to the highest austenite content, as shown in Fig. 1. In the present study, we further study the effect of various aging times at 650 °C on hydrogen-assisted crack using slow strain rate tensile tests. In addition, the hydrogen-induced crack nucleation and crack growth mechanism are analyzed and discussed.

2. Experimental method

2.1. Test material preparation and microstructure analysis

The chemical composition in weight percent of the PH 13-8 Mo martensitic stainless steel is shown in Table 1. The cylindrical bars with a diameter of 20 mm were solution-treated at 925 °C for 1 h and then oil-

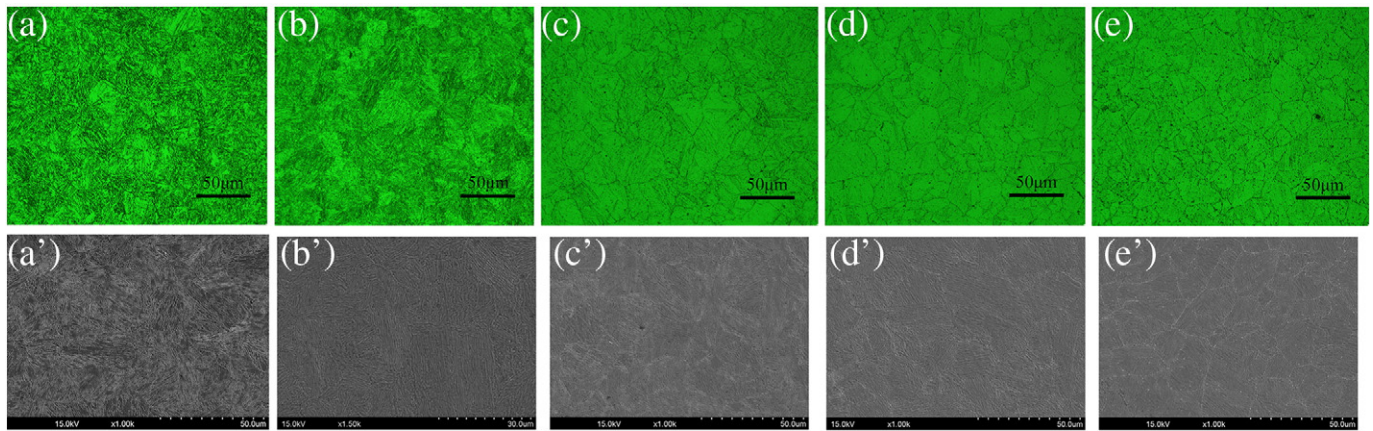


Fig. 2. Microstructure of specimens aged at 650 °C for various aging times. (a) and (a') 0.5 h; (b) and (b') 4 h; (c) and (c') 10 h; (d) and (d') 30 h, (e) and (e') 78.5 h.

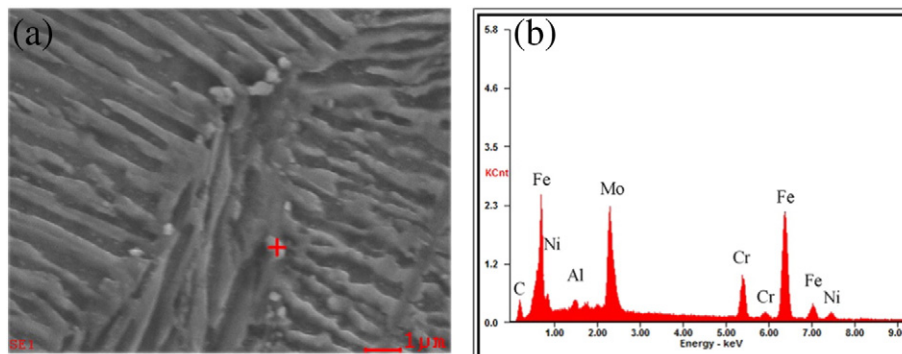


Fig. 3. (a) SEM micrographs of specimens aged at 650 °C for 78.5 h and (b) EDS peaks from a carbide showing Mo and Cr as the main elements.

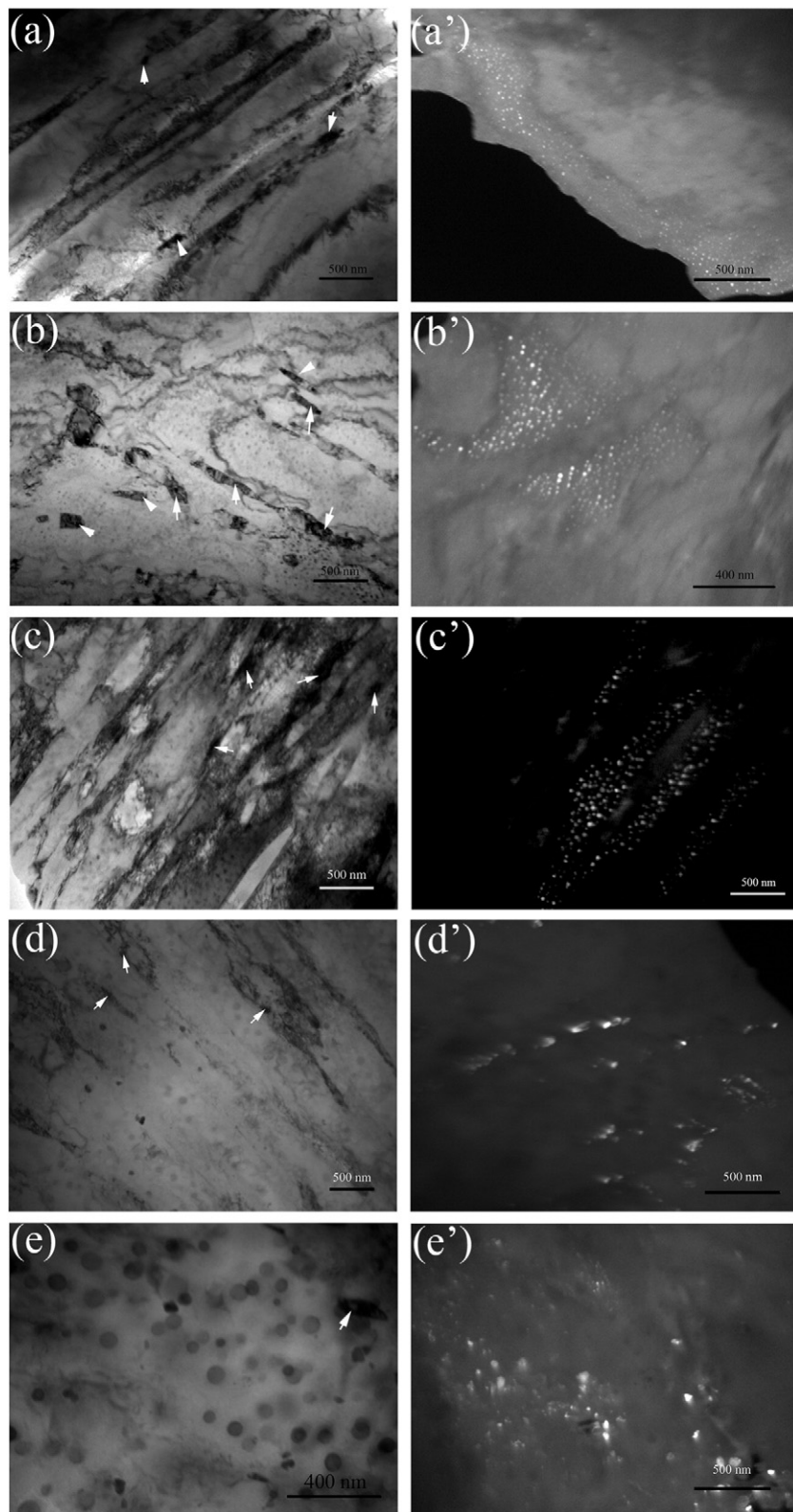


Fig. 4. TEM micrographs of the specimens aged at 650 °C for various aging times. (a) bright field (BF) image and (a') dark field (DF) image taken from NiAl precipitates for 0.5 h; (b) BF image and (b') DF image taken from NiAl precipitates for 4 h; (c) BF image and (c') DF image taken from NiAl precipitates for 10 h; (d) BF image and (d') DF image taken from NiAl precipitates for 30 h; (e) BF image and (e') DF image taken from NiAl precipitates for 78.5 h. White arrows indicate the austenitic phase.

cooled to room temperature (298 K). Subsequently, the bars were subjected to aging treatment at 650 °C for 0.5 h, 4 h, 10 h, 30 h and 78.5 h. After aging treatment, smooth tensile specimens with a diameter of 5 mm and a gauge length of 25 mm were machined, mechanically

ground from 180 to 800 grit silicon carbide papers and then rinsed with alcohol.

The alloy was etched with a mixture solution of 100 g FeCl₃, 200 mL HCl and 1000 mL H₂O and then observed by an optical microscope (OM)

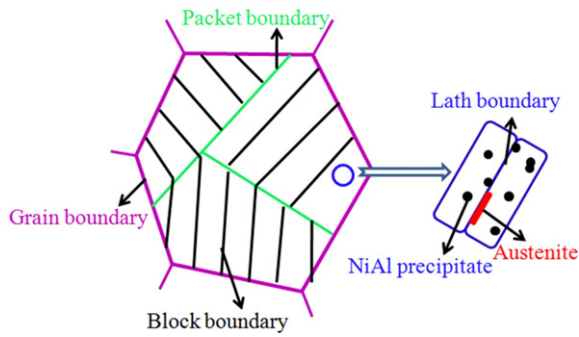


Fig. 5. Schematic illustration of the microstructure for the sample aged at 650 °C for 4 h.

and scanning electron microscopy (SEM) with an energy dispersive spectrometer (EDS) for microstructural determinations. Transmission electron microscopy (JEM-200CX TEM) operating at 120 kV was used to investigate the sub-microstructures. Some thin sheet samples for TEM observation were cut from the alloy, mechanically ground and then electrochemically thinned by a twin-jet machine in 10 vol.(%) perchloric acid and 90 vol.(%) ethanol solution at -30°C . In addition, the microstructures of the steel were also studied by using an X-ray

diffractometer (XRD) with a Cu K α target operated at 40 kV. The scanning range, rate and step size were from 40° to 120° , 6°min^{-1} and 0.02° , respectively. The volume fraction of austenite was evaluated by comparison of the integrated intensities of the martensite and austenite peaks [13].

2.2. Electrochemical hydrogen-charging tests

Hydrogen was introduced into the tensile specimens by electrochemical charging method. Specimens were hydrogen-charged in a $0.5\text{ mol L}^{-1}\text{H}_2\text{SO}_4$ solution at a constant current density of 0.15 mA cm^{-2} for 24 h at room temperature. Thiourea ($\text{CH}_4\text{N}_2\text{S}$ 1 g L^{-1}) was added in the solution to decrease hydrogen atom recombination and to increase hydrogen adsorption on the surfaces of specimens. The specimens were used as a cathode and the platinum was used as an anode. In order to ensure that only the gauge section of the specimens was charged with hydrogen, the surfaces of the other parts were covered with paraffin.

2.3. Cadmium electroplating tests

To prevent hydrogen release during tensile tests, all pre-charged specimens were electroplated with a cadmium coating [7,14]. Cadmium

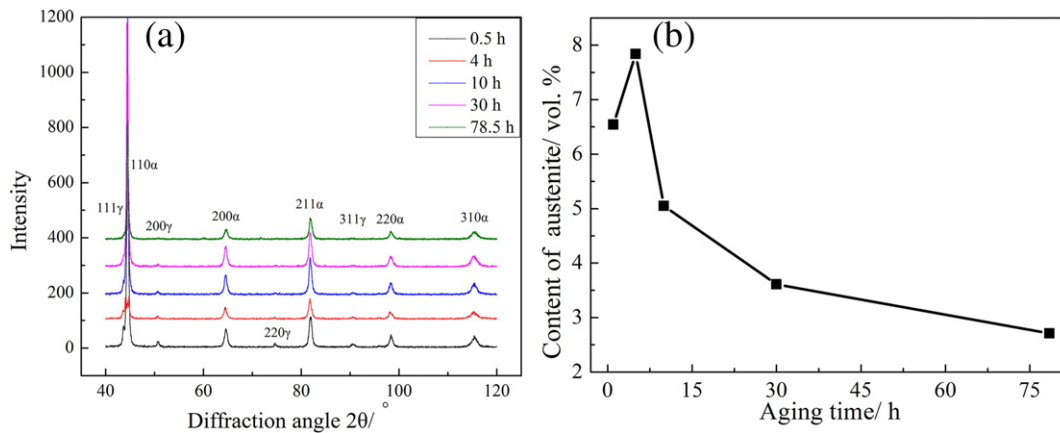


Fig. 6. (a) X-ray diffraction patterns of the samples aged at 650 °C for various aging times. (b) Relationship between aging time and content of austenite.

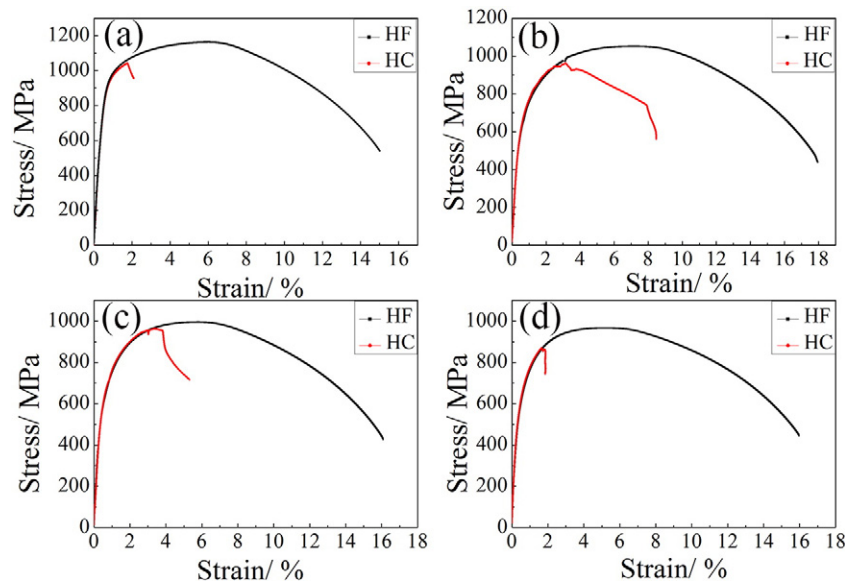


Fig. 7. Stress-strain curves of hydrogen-free (HF) and hydrogen-charged (HC) specimens aged at 650 °C for different times. (a) 0.5 h, (b) 4 h, (c) 10 h and (d) 30 h.

Table 2

Mechanical properties of hydrogen-free (HF) and hydrogen-charged (HC) specimens aged at 650 °C for different aging time.

Aging time/h		Yield strength/MPa	Tensile strength/MPa	Reduction of area/%	HEI/%	Brittle zone depth/ μm	Ratio of brittle zone to the radius/%
0.5	HF	914.94	1163.49	74.17	88.93	783	31.32
	HC	927.04	1042.89	8.21			
4	HF	657.86	1051.93	77.53	63.33	480	19.2
	HC	685.95	961.71	28.43			
10	HF	644.97	996.08	77.13	87.38	569	22.76
	HC	667.30	962.48	9.73			
30	HF	663.24	967.89	73.36	90.91	711	28.44
	HC	673.24	869.89	6.67			
78.5	HF	635.67	952.80	72.54	92.40	942	37.68
	HC	665.71	916.59	5.51			

plating tests were performed in an aqueous solution with 98% oil of vitriol (50 g L^{-1}), CdSO_4 powder (50 g L^{-1}), Na_2SO_4 (45 g L^{-1}), glutin (6 g L^{-1}) and phenol (3 g L^{-1}) at the current density of 25 mA cm^{-2} for 5 min. The cadmium was served as an anode while the specimens were used as a cathode.

2.4. Slow strain rate tensile tests

Following cadmium electroplating, slow strain rate tensile tests were immediately performed using an Instron 1195 universal testing machine with a constant crosshead speed of 0.03 mm min^{-1} , corresponding to a normal tensile rate of $2 \times 10^{-5} \text{ s}^{-1}$. Moreover, the specimens without hydrogen charging were also tensile tested as references. The index of relative susceptibility to hydrogen embrittlement (HEI) of specimens was determined by measuring the relative plasticity loss of the specimens, which can be expressed as:

$$\text{HEI} = \frac{\varphi_0 - \varphi_H}{\varphi_0} \times 100\% \quad (1)$$

where φ_0 and φ_H were the reduction of area of hydrogen-free (HF) and hydrogen-charged (HC) specimens, respectively.

After tensile tests, the fracture surfaces were subjected to a detailed analysis by SEM. In addition, the samples normal to the fracture surfaces were extracted by wire electrical discharge machining, mechanical polished, etched and then investigated near the fracture surface region by SEM in order to unravel underlying crack nucleation and propagation mechanism.

3. Results

3.1. Microstructure

Fig. 2(a)–(e) presents the optical micrographs of the specimens aged at 650 °C for various aging times. All microstructures are composed of tempered martensite, which is also demonstrated by SEM observation, as shown in Fig. 2(a')–(e'). For the specimens aged at 10 h, 30 h and 78.5 h, spherical carbides both in grain interiors and grain boundaries are observed, as shown in Fig. 2(c)–(e), respectively. The quantity of carbides increases with an increase in aging time. Fig. 3 exhibits EDS peak in a specimen aged at 650 °C for 78.5 h, revealing that Mo and Cr are the main elements in the carbide.

TEM micrographs of the specimens aged at various aging times are shown in Fig. 4(a)–(e). The microstructures of all specimens consist of a lath martensite structure with elongated or granular shape austenite grain (indicated by a white arrow) along lath boundaries and a nano-sized precipitated NiAl phase is also observed within the lath martensite matrix. For low-carbon steel martensite, the prior austenite grain is divided into packets that are groups of parallel laths with the same habit plane. The packet is divided by several blocks, which are parallel lath with the same crystal orientation. A schematic illustration of the microstructure for the sample aged at 650 °C for 4 h is present as Fig. 5.

As the aging time increases, dislocation density decreases, which is attributed to recovery mechanism, and the size of NiAl precipitates increases, as indicated by TEM dark field images in Fig. 4(a')–(e'). When the aging time is short ($<10 \text{ h}$), the size of NiAl precipitates is small and homogeneous, while a variety of sizes of NiAl precipitates are observed in long aging time ($>30 \text{ h}$). The relationship between aging time and content of austenite is given in Fig. 6. With an increase in aging time, the content of austenite firstly increases, reaches the

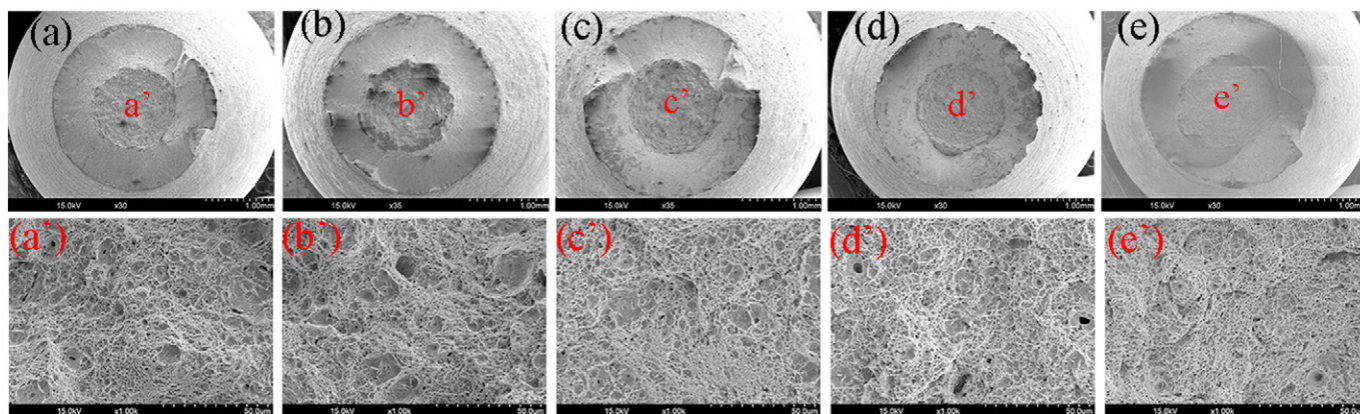


Fig. 8. SEM micrographs of hydrogen-free specimens aged at 650 °C for various aging times. (a) 0.5 h, (a') magnified area indicated in (a); (b) 4 h, (b') magnified area indicated in (b); (c) 10 h, (c') magnified area indicated in (c); (d) 30 h, (d') magnified area indicated in (d); (e) 78.5 h, (e') magnified area indicated in (e).

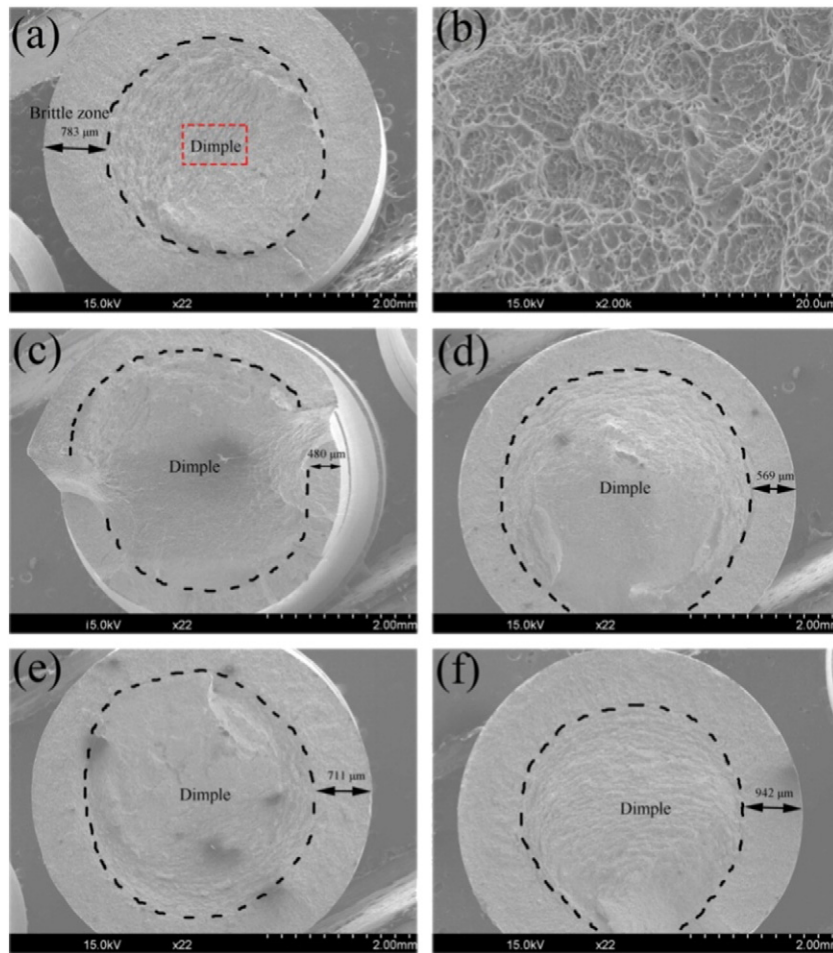


Fig. 9. SEM micrographs of hydrogen-charged specimens aged at 650 °C for various aging times. (a) 0.5 h, (b) magnified area indicated in the red dotted square in (a), (c) 4 h, (d) 10 h, (e) 30 h and (f) 78.5 h.

maximum value for 4 h and then decreases, which is consistent with TEM observation.

3.2. Mechanical properties

Stress-strain curves of HF and HC specimens aged at 650 °C for different time are shown in Fig. 7. For all HF specimens, the stress firstly increases, reaches the peak value and then decreases as the strain increases. However, the fracture strain of HC specimens is shortened in comparison with those of HF specimens, especially for the specimens aged for 0.5 h and 30 h, implying serious hydrogen embrittlement sensitivity.

Mechanical properties of HF and HC specimens are listed in Table 2. Hydrogen charging slightly increases 0.2% offset yield strength and decreases tensile strength. However, hydrogen reduces the reduction of area dramatically in comparison with that of HF specimen. With increasing aging time, HEI firstly decreases and then increases.

3.3. SEM observation

3.3.1. Fracture morphology

Fig. 8(a)–(e) exhibits the macroscopic fracture morphology of HF specimens aged at various aging times, showing typical ductile fractures. They fracture along about 90° of the direction of tensile load with severe necking. Corresponding high magnification images reveal dimple fracture mode, as shown in Fig. 8(a')–(e'). HC specimens, as shown in Fig. 9, present relatively less necking, which implies a loss of ductility due to hydrogen. Further, a little necking is observed in the

specimen aged at 650 °C for 4 h, while other aging time samples show no necking and macroscopic flat fracture surfaces are almost perpendicular to the tensile direction. Two zones with distinctly different features can be observed. The zone near the edge of fracture surface shows brittle fracture feature, which is attributed to high hydrogen concentration near surface during electrochemical hydrogen charging, as shown in Fig. 9(a), (c), (d), (e) and (f), whereas the central zone exhibits dimple fracture, as shown in Fig. 9(b). Moreover, the depth sizes of brittle zone, i.e., the distance from the specimen surface to the brittle-ductile junction, are 783 μm, 480 μm, 569 μm, 711 μm, and 942 μm when the specimens aged for corresponding aging times of 0.5 h, 4 h, 10 h, 30 h and 78.5 h, as listed in Table 2.

High magnification images of brittle zone for samples aged at various times are shown in Fig. 10. The fracture characteristics are mainly intergranular fracture (IG) with some quasi-cleavage fracture (QC) features, as shown in Fig. 10(a), (b) and (c). Intergranular cracks (indicated by white arrows), tearing ridges (indicated by white dotted circle) and micropores (indicated by a black dotted circle) on the grain boundary are detected, as shown in Fig. 10(a'), (b') and (c'), which are typical characteristics of hydrogen embrittlement for high strength steels [15,16]. In addition, triple junctions (indicated by red dotted circles) of grain boundaries exhibit intergranular cracking. It is interesting that more and deeper dimples are produced on facets along grain boundaries for the specimens aged for 30 h and 78.5 h in comparison with those of specimen aged for 0.5 h. This may be attributed to the case that grain boundaries are hydrogen traps and that more and larger carbides are located at grain boundaries, as shown Fig. 2(c)–(e).

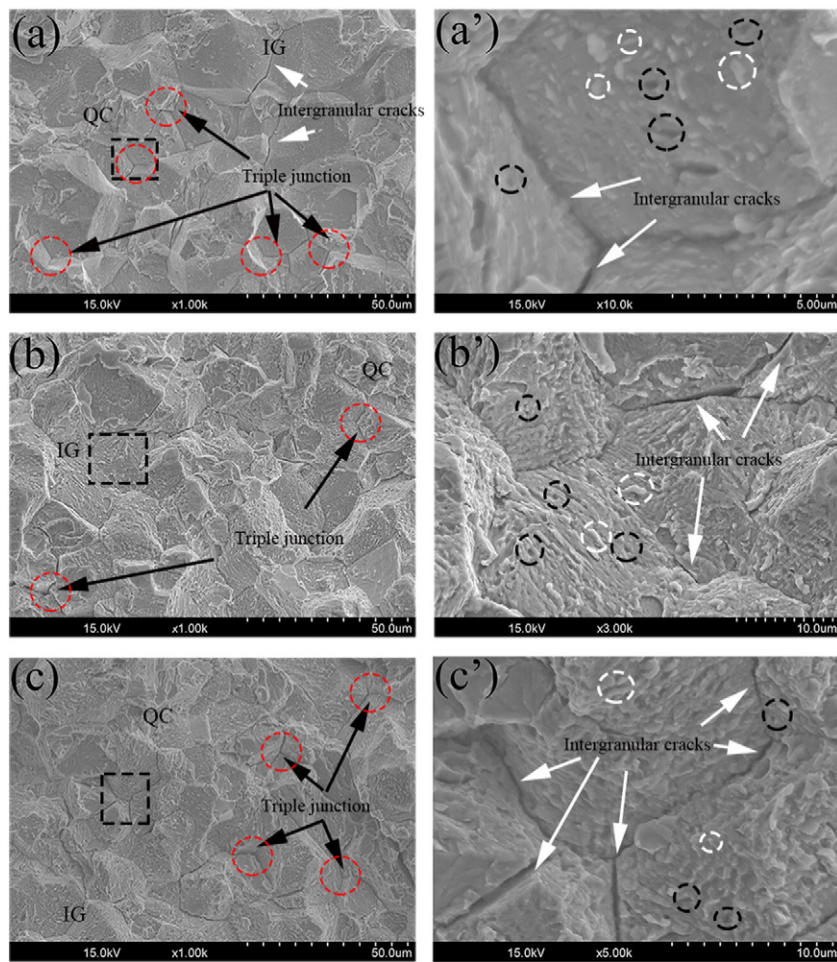


Fig. 10. SEM micrographs of brittle zone in HC specimens aged at 650 °C for various aging time. (a) 0.5 h, (a') magnified area indicated in the black dotted square in (a); (b) 30 h, (b') magnified area indicated in the dotted square in (b); (c) 78.5 h, (c') magnified area indicated in the dotted square in (c). White arrows show intergranular cracks. Black arrows show triple junction. White dotted circles indicate tearing ridges. Black dotted circles indicate micropores. IG: intergranular fracture. QC: quasi-cleavage fracture.

3.3.2. Hydrogen-induced crack initiation and propagation

Hydrogen-induced crack in the sample aged at 650 °C for 4 h is shown in Fig. 11. Two kinds of crack nucleation sites are observed, either along lath boundaries or along prior austenite grain boundaries, as shown in Fig. 11(a) and (d), respectively, while NiAl precipitates are also observed within martensite lath. When the observation is moved towards fracture surface, corresponding to an increase in strain, the area fraction of the crack increases. The fresh small cracks are located at different lath boundaries (Fig. 11(b)) or at prior austenite grain boundaries in the front of the main crack (Fig. 11(e)). After linking with these small cracks, the main crack passes through the lath boundaries and walks along grain boundaries, as shown in Fig. 11(c) and (f), respectively. In addition, the elongated and bent martensitic lath is observed near the fracture surface region, as shown in Fig. 12, implying that an extensive plastic deformation occurs, although the fracture surface exhibits brittle intergranular and quasi-cleavage fracture mode (Fig. 10). This result is in accordance with references [17].

Fig. 13 shows a hydrogen-induced crack in the sample aged at 650 °C for 30 h. The crack nucleation sites and crack growth process are similar to those of the sample aged for 4 h. Moreover, the cracks along the packet boundaries also occur for the sample aging time 4 h and 30 h, as shown in Fig. 14(a) and (b), respectively, indicating that packet boundaries act as another crack initiation sites, whereas the crack initiation from the carbide is not observed.

4. Discussion

4.1. Effect of hydrogen on yield strength and tensile strength of PH 13-8 Mo steel

The influence of hydrogen on yield strength of steels has been widely investigated. However, the results are inconclusive. A study [18] reported that hydrogen had no effect on yield strength of low alloy steel, silicon steel and low-carbon steel. However, Dubovoi et al. [19] revealed that yield strength in pearlitic steel increased with increasing hydrogen content when hydrogen concentration was over 2.5 ppm. Moreover, Chu et al. [20] found that yield strength decreased for 20 steel, increased for 45 steel as well as 30CrMnSiNi steel and did not change for 40Cr and 32SiMnMoV steel after hydrogen charging. In the present study, hydrogen slightly increases yield strength, as shown in Table 2, which can be due to the case that hydrogen or hydrogen clusters act as solute hardeners and inhibit the movement of dislocations in the peripheral brittle zone on the basis of previous reports [21–24]. Abraham et al. [21] found that typical hardening per At. Pct of Solute due to hydrogen was G/2000 while the hardening effect of carbon and nitrogen was G/1200 and G/800, respectively, in austenitic stainless steel. Internal friction study suggested that clusters or atmospheres of hydrogen interacted with dislocations and may be involved in strengthening the austenite [22]. Zhao et al. [23] reported that electrochemical hydrogen charging led to the formation of hydrogen atmospheres around dislocations, which pinned the dislocations and increased the plastic deformation stress. In

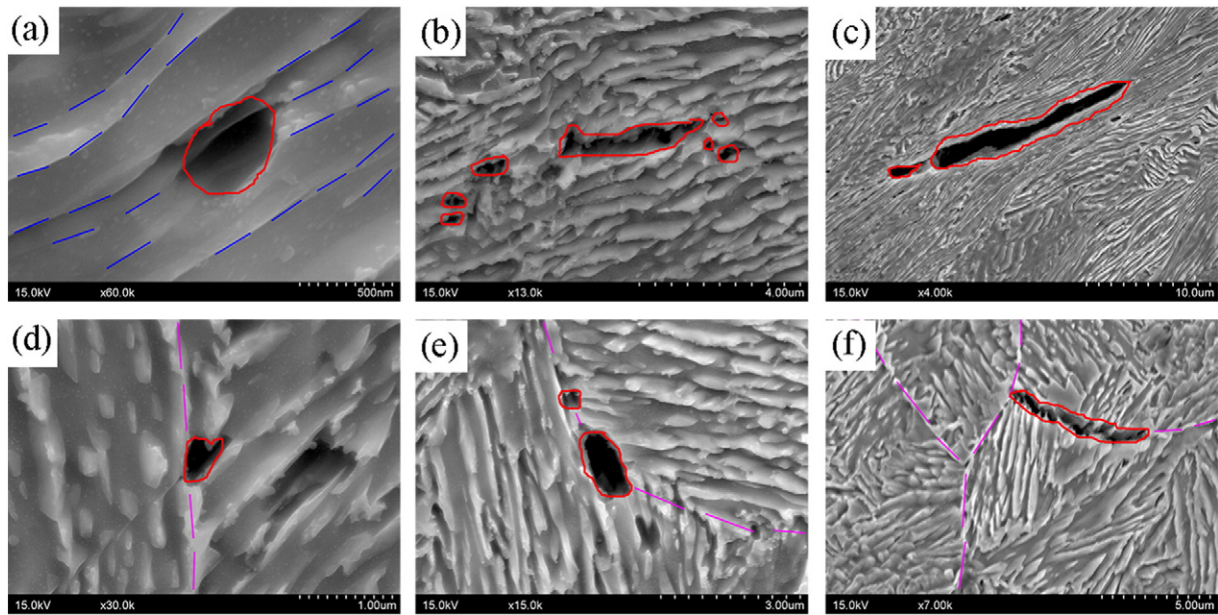


Fig. 11. Hydrogen-induced crack in the sample aged at 650 °C for 4 h. (a) crack initiation at lath boundaries; (b) crack coalescence at lath boundaries; (c) crack passing through lath boundaries; (d) crack initiation at prior austenite grain boundaries; (e) crack coalescence at grain boundaries; (f) crack along grain boundaries. Blue dotted line shows lath boundaries. Pink dotted line shows prior austenite grain boundaries. Red line indicates cracks.

addition, Song and Curtin [24] revealed that hydrogen in α -iron generated Cottrell atmosphere, which led to a resistance to dislocation motion.

In the presence of hydrogen, tensile strength decreases, as listed in Table 2. The hydrogen-enhanced decohesion (HEDE) mechanism, which was proposed by Pfeil [25], developed by Oriani [26] and they supposed that hydrogen decreased the cohesion strength across cleavage planes and grain boundaries, is responsible for the reduction of tensile strength. Yamaguchi et al. [27] evaluated the cohesion energy of a specified grain boundary decorated with hydrogen atoms by theoretical simulation using the first principle calculation and revealed that the cohesive energy was decreased by 40% under the effect of immobile hydrogen. According to their results, taking the effect of mobile hydrogen into consideration, the cohesive energy was decreased by about 70–80%. Furthermore, preferential crack nucleation sites at the lath, packet and prior austenite grain boundaries, as shown in Figs. 11, 13 and 14, and intergranular fracture as well as triple junctions intergranular cracks, as shown in Fig. 10, are observed in the brittle zone of HC specimens, indicating that the reduction in cohesive strength of these boundaries could be greater than that of matrix after hydrogen charging.

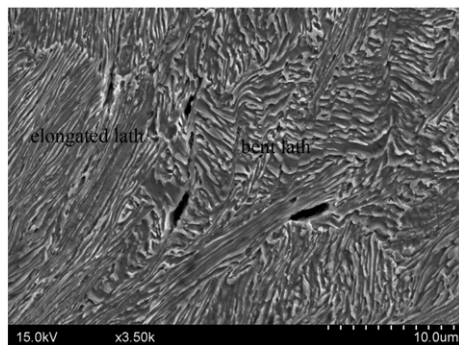


Fig. 12. Elongated and bent martensite lath near the fracture surface of the sample aged at 650 °C for 4 h.

4.2. Effect of aging time on hydrogen embrittlement susceptibility of PH 13-8 Mo steel

With an increase in aging time, HEI firstly decreases and then increases. This is related with hydrogen diffusivity behaviors during hydrogen charging. Increasing aging time reduces dislocation density (Fig. 4), increases carbide (Fig. 1) and NiAl precipitate size (Fig. 3) and causes the variation of austenite phase content. Decreased dislocation hydrogen traps increase hydrogen permeation, whereas the formation of carbides decreases hydrogen diffusivity. A study [28] reported that the apparent hydrogen diffusivity coefficient decreased from $2.60 \times 10^{-11} \text{ m s}^{-2}$ to $1.75 \times 10^{-11} \text{ m s}^{-2}$ as the degree of pre-strain varied from 0% to 4% pre-strain. Shen et al. [29] reported that M_{23}C_6 carbide reduced hydrogen diffusion coefficient, leading to higher notch tensile strength of the 3/4R samples. Wang et al. [30] revealed that hydrogen diffusion coefficient for 600 °C tempered sample ($3.93 \times 10^{-11} \text{ m s}^{-2}$) was larger than that for 630 °C tempered sample ($3.63 \times 10^{-11} \text{ m s}^{-2}$), which was due to less carbides irreversible hydrogen traps. In addition, Xie et al. [31] reported that with increasing Ni_3Ti precipitates size (from 10.4 nm to 36.8 nm) in TM210 maraging steel, corresponding hydrogen diffusion coefficient increased from $3.34 \times 10^{-13} \text{ m}^2 \text{ s}^{-1}$ to $6.52 \times 10^{-13} \text{ m}^2 \text{ s}^{-1}$. This fact implies that with the reduction of precipitates size the diffusivity of hydrogen in steels decreases. Most important, the ferritic phase is a body centred cubic (bcc) structure, showing a high diffusion rate ($1.5 \times 10^{-11} \text{ m s}^{-2}$) and a low solubility due to its open lattice structure. In contrast, the austenite phase is a face centred cubic structure, giving a low diffusion rate ($1.4 \times 10^{-16} \text{ m s}^{-2}$) and a high solubility due to its close packed lattice. Hence, the increase in austenite content in steel can retard hydrogen diffusivity significantly. A study [11] reported that hydrogen diffusion coefficient in the H1100 specimen ($2.48 \times 10^{-13} \text{ m}^2 \text{ s}^{-1}$) of PH 13-8 Mo steel was one order less than that of other condition ($\sim 2 \times 10^{-12} \text{ m}^2 \text{ s}^{-1}$), while apparent hydrogen solubility (2960 mol m^{-3}) was six times higher than that of others ($\sim 500 \text{ mol m}^{-3}$). This was attributed to an increase in the amount of austenite in the H1100 specimen. The hydrogen permeation is lowest in austenite phase and is dominantly affected by austenite content,

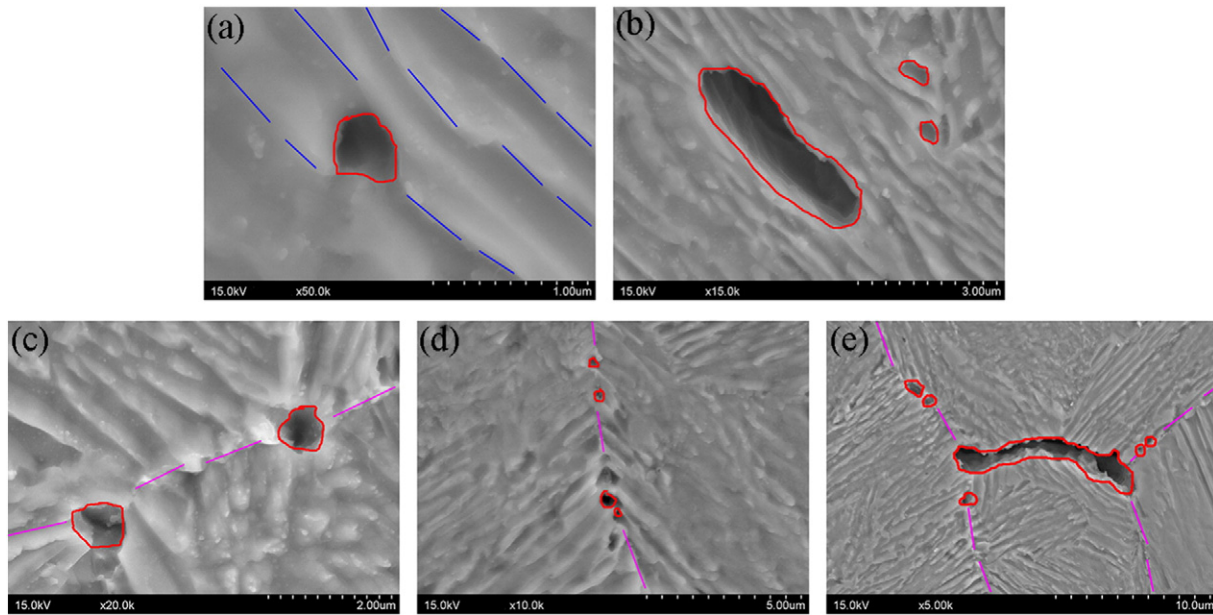


Fig. 13. Hydrogen-induced crack in the sample aged at 650 °C for 30 h. (a) crack initiation at lath boundaries; (b) crack coalescence at lath boundaries; (c) crack initiation at prior austenite grain boundaries; (d) crack coalescence at grain boundaries; (f) crack along grain boundaries. Blue dotted line shows lath boundaries. Pink dotted line shows prior austenite grain boundaries. Red line indicates cracks.

which is in accordance with the references [7,9,11,12], when compared with dislocations, carbides and NiAl precipitate hydrogen traps. For HC sample aged for 4 h, the highest austenite content is observed and hydrogen permeation behaviors can be effectively reduced, which is demonstrated by the smallest size of brittle zone, resulting in the lowest HEI.

4.3. Effect of hydrogen on crack nucleation and propagation of PH 13-8 Mo steel

For the sample aged at 650 °C for 4 h and 30 h, hydrogen-induced crack nucleation or propagation is along the interfaces of lath, packet, and prior austenite grain, as shown in Figs. 11, 13 and 14, leading to transgranular fracture and intergranular fracture (Fig. 10). On the one hand, the hydrogen-induced crack is attributed to HEDE mechanism. During tensile deformation, the dislocations motion can be triggered. At the low strain rate ($2 \times 10^{-5} \text{ s}^{-1}$), hydrogen can migrate via moving dislocations. When the dislocations meet the obstacles, they will interact with them. It is reported that internal boundaries in lath martensite, such as lath, block and packets within prior grain, serve as potential barriers to dislocation motion [32]. The dislocation motion is also inhibited by precipitates [1,33,34], such as carbides and NiAl precipitates. The dislocations interact with and incorporate in these boundaries and precipitates, and the process of slip transmission creates a new dislocation. In this process, hydrogen can be deposited at the interfaces between

matrix and obstacles in the case of slip transferring through obstacles due to weak hydrogen traps of dislocations ($\sim 26 \text{ kJ mol}^{-1}$), resulting in hydrogen accumulation at the lath martensite boundaries and interfaces between matrix and precipitates. Further, when the dislocations transfer across the obstacles, the numbers of incoming and outgoing dislocations are not one-to-one and many dislocations can be accommodated within interfaces between matrix and obstacles before one is emitted from it [35]. The dislocation pileups lead to the formation of local work hardening, further resulting in hydrogen accumulation at the interfaces between matrix and obstacles under the role of stress gradient. It is well-established that local cohesive stress is inversely proportional to the accumulated hydrogen concentration. Compared with carbide and NiAl precipitates, the hydrogen-induced reduction in cohesive stress on lath, packet and prior austenite grain boundaries prevails, causing cracks to initiate from at lath, packet and prior austenite grain boundaries. On the other hand, elongated and granular austenite along the lath boundaries (indicated by a white arrow in Fig. 4) is responsible for crack initiation. Chan et al. [36] pointed out that the austenite/martensite interfaces acted as preferential hydrogen traps sites. In addition, Wang et al. [37] reported that hydrogen-induced crack occurred at the interfaces between matrix martensite and austenite. During tensile deformation the freshly formed martensite from retained austenite, which has a higher hydrogen solubility in comparison with martensite, will be supersaturated with hydrogen, causing crack

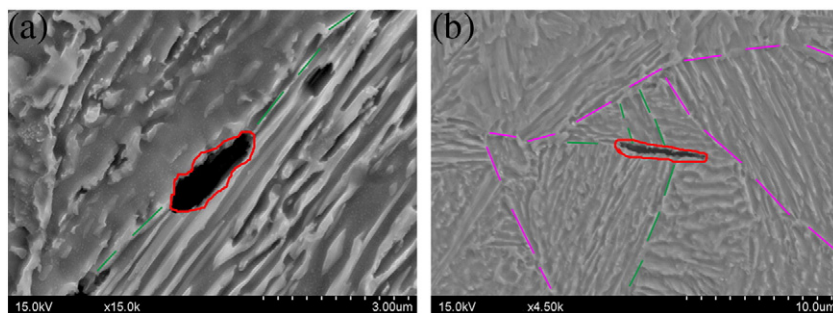


Fig. 14. Hydrogen-induced crack along the packet boundaries in the sample aged at 650 °C for (a) 4 h; (b) 30 h. Green dotted line shows packet boundaries. Pink dotted line shows prior austenite grain boundaries. Red line indicates cracks.

initiation from lath boundaries. Subsequently, by linking small cracks located in lath, packet and grain boundaries, the crack grows and propagates through lath boundaries or along packet and prior austenite grain boundaries.

5. Conclusion

In this study, the effect of hydrogen on tensile properties and fracture behavior of PH 13–8 Mo steel was investigated by combined cathodically hydrogen charging and slow strain rate tensile experiments. Following conclusions are obtained.

- (1) Hydrogen slightly increases yield strength, which can be attributed to the fact that hydrogen or hydrogen clusters act as solute hardeners and inhibit the movement of dislocations in the peripheral brittle zone. However, hydrogen decreases tensile strength due to HEDE mechanism.
- (2) As the aging time increases, the susceptibility to hydrogen embrittlement of specimens aged at 650 °C firstly decreases and then increases, reaching the highest resistance to hydrogen embrittlement for the sample aged for 4 h. This is dominantly attributed to high content of austenite, which can reduce greatly the entry of hydrogen into the steel. In addition, on the basis of our previous result (Fig. 1), it is suggested that the increase in austenite content is feasible to improve the resistance to hydrogen embrittlement.
- (3) Hydrogen-induced crack nucleation sites are located at the lath, packet and prior austenite grain boundaries. Crack propagation passes through the lath boundaries and walks along packet and prior austenite grain boundaries.
- (4) SEM micrographs reveal that hydrogen-free specimens show dimple fracture while quasi-cleavage fracture and intergranular fracture are observed in hydrogen-charged specimen annular brittle zone.

Acknowledgments

The authors acknowledge the help of T. J. Wang and G. X. Yang for providing the PH 13–8 Mo steel materials. X. F. Li would like to acknowledge financial support by the Doctoral Research Assistant Foundation of Xi'an Jiaotong University.

References

- [1] R. Schnitzer, G.A. Zickler, E. Lach, H. Clemens, S. Zinner, T. Lippmann, et al., Influence of reverted austenite on static and dynamic mechanical properties of a PH 13–8 Mo maraging steel, *Mater. Sci. Eng. A* 527 (2010) 2065–2070.
- [2] D. Sen, A.K. Patra, S. Mazumder, J. Mitra, G.K. Dey, P.K. De, Morphology of carbide precipitates in solution quenched PH13–8 Mo stainless steel: a small-angle neutron scattering investigation, *Mater. Sci. Eng. A* 397 (2005) 370–375.
- [3] V. Seetharaman, M. Sundararaman, R. Krishnan, Precipitation hardening in a PH 13–8 Mo stainless steel, *Mater. Sci. Eng.* 47 (1981) 1–11.
- [4] D.H. Ping, M. Ohnuma, Y. Hiraoka, Y. Kadoya, K. Hono, Microstructural evolution in 13Cr–M–2.5Mo–2Al martensitic precipitation-hardened stainless steel, *Mater. Sci. Eng. A* 394 (2005) 285–295.
- [5] C.V. Robino, M.J. Cieslak, P.W. Hochanadel, G.R. Edwards, Heat treatment of investment cast PH 13–8 Mo stainless steel: part II. Isothermal aging kinetics, *Metall. Mater. Trans. A* 25 (1994) 697–704.
- [6] P.D. Bilmes, M. Solari, C.L. Llorente, Characteristics and effects of austenite resulting from tempering of 13Cr–NiMo martensitic steel weld metals, *Mater. Charact.* 46 (2001) 285–296.
- [7] X. Li, J. Zhang, J. Chen, S. Shen, G. Yang, T. Wang, et al., Effect of aging treatment on hydrogen embrittlement of PH 13–8 Mo martensitic stainless steel, *Mater. Sci. Eng. A* (2015).
- [8] R. Schnitzer, R. Radis, M. Nohrer, M. Schober, R. Hochfellner, S. Zinner, et al., Reverted austenite in PH 13–8 Mo maraging steels, *Mater. Chem. Phys.* 122 (2010) 138–145.
- [9] Y.S. Ding, L.W. Tsay, M.F. Chiang, C. Chen, Gaseous hydrogen embrittlement of PH 13–8 Mo steel, *J. Nucl. Mater.* 385 (2009) 538–544.
- [10] L.M. Young, M.R. Eggleston, H.D. Solomon, L.R. Kaisand, Hydrogen-assisted cracking in a precipitation-hardened stainless steel: effects of heat treatment and displacement rate, *Mater. Sci. Eng. A* 203 (1995) 377–387.
- [11] L.W. Tsay, M.Y. Chi, H.R. Chen, C. Chen, Investigation of hydrogen sulfide stress corrosion cracking of PH 13–8 Mo stainless steel, *Mater. Sci. Eng. A* 416 (2006) 155–160.
- [12] L.W. Tsay, H.H. Chen, M.F. Chiang, C. Chen, The influence of aging treatments on sulfide stress corrosion cracking of PH 13–8 Mo steel welds, *Corros. Sci.* 49 (2007) 2461–2473.
- [13] D.-S. Leem, Y.-D. Lee, J.-H. Jun, C.-S. Choi, Amount of retained austenite at room temperature after reverse transformation of martensite to austenite in an Fe–13%Cr–7%Ni–3%Si martensitic stainless steel, *Scr. Mater.* 45 (2001) 767–772.
- [14] X. Li, Y. Wang, P. Zhang, B. Li, X. Song, J. Chen, Effect of pre-strain on hydrogen embrittlement of high strength steels, *Mater. Sci. Eng. A* 616 (2014) 116–122.
- [15] D. Sasaki, M. Koyama, S. Hamada, H. Noguchi, Tensile properties of precracked tempered martensitic steel specimens tested at ultralow strain rates in high-pressure hydrogen atmosphere, *Philos. Mag. Lett.* 1–9 (2015).
- [16] J.A. Wang, F. Ren, T. Tan, K. Liu, The development of in situ fracture toughness evaluation techniques in hydrogen environment, *Int. J. Hydrog. Energy* 40 (2015) 2013–2024.
- [17] A. Nagao, C.D. Smith, M. Dadfarnia, P. Sofronis, I.M. Robertson, The role of hydrogen in hydrogen embrittlement fracture of lath martensitic steel, *Acta Mater.* 60 (2012) 5182–5189.
- [18] W. Zhu, *Hydrogen Embrittlement and Stress Corrosion Cracking*: Science Press, 2013.
- [19] M. Smialowski, Chapter 12—flakes (hair-line cracks) produced by hydrogen in steel*, *Hydrogen in Steel* 1962, pp. 327–346.
- [20] W.Y. Chu, S.Q. Li, C.M. Hsiao, S.Y. Ju, Effect of hydrogen on the apparent yield stress—research on the cause of hydrogen induced delayed plasticity, *Corrosion (Houston TX)* 37 (1981) 514–521.
- [21] D.P. Abraham, C.J. Altstetter, The effect of hydrogen on the yield and flow stress of an austenitic stainless steel, *Metall. Mater. Trans. A* 26 (1995) 2849–2858.
- [22] K. Tanaka, T. Inukai, K. Uchida, M. Yamada, Dislocation relaxation peaks involving hydrogen drag in deformed Ni–H alloys, *J. Appl. Phys.* 54 (1983) 6890–6896.
- [23] Y. Zhao, M.Y. Seok, I.C. Choi, Y.H. Lee, S.J. Park, U. Ramamurty, et al., The role of hydrogen in hardening/softening steel: influence of the charging process, *Scr. Mater.* 107 (2015) 46–49.
- [24] J. Song, W.A. Curtin, Mechanisms of hydrogen-enhanced localized plasticity: an atomistic study using α -Fe as a model system, *Acta Mater.* 68 (2014) 61–69.
- [25] L. Pfeil, The effect of occluded hydrogen on the tensile strength of iron, *Proceedings of the Royal Society of London Series A, Containing Papers of a Mathematical and Physical Character* 1926, pp. 182–195.
- [26] R. Oriani, A mechanistic theory of hydrogen embrittlement of steels, *Ber. Bunsenges. Phys. Chem.* 76 (1972) 848–857.
- [27] M. Yamaguchi, K.-I. Ebihara, M. Itakura, T. Kadoyoshi, T. Suzudo, H. Kaburaki, First-principles study on the grain boundary embrittlement of metals by solute segregation: part II. Metal (Fe, Al, Cu)–hydrogen (H) systems, *Metall. Mater. Trans. A* 42 (2011) 330–339.
- [28] X. Li, J. Zhang, Y. Wang, B. Li, P. Zhang, X. Song, Effect of cathodic hydrogen-charging current density on mechanical properties of prestrained high strength steels, *Mater. Sci. Eng. A* 641 (2015) 45–53.
- [29] K. Shen, L. Xu, Y. Guo, J. Shi, M. Wang, Effect of microstructure on hydrogen diffusion and notch tensile strength of large steel forging, *Mater. Sci. Eng. A* 628 (2015) 149–153.
- [30] S. Wang, X. Cheng, P. Feng, University S, Effect of tempering temperature on hydrogen diffusion behaviors in mooring chain steel of level R5, *Heat Treat. Met.* (2013).
- [31] C.Q. Xie, J.X. Li, Q. Li, Z. Zhang, Y.J. Su, L.J. Qiao, Effect of precipitate on hydrogen diffusion coefficient of TM210 maraging steel, *Cailiao Rechuli Xuebao/Trans. Mater. Heat Treat.* 35 (2014) 33–39.
- [32] C. Du, J.P.M. Hoefnagels, R. Vaes, M.G.D. Geers, Block and sub-block boundary strengthening in lath martensite, *Scr. Mater.* 116 (2016) 117–121.
- [33] T. Ohmura, T. Hara, K. Tsuzaki, Evaluation of temper softening behavior of Fe–C binary martensitic steels by nanoindentation, *Scr. Mater.* 49 (2003) 1157–1162.
- [34] X. Shi, W. Yan, W. Wang, Y. Shan, K. Yang, Novel Cu-bearing high-strength pipeline steels with excellent resistance to hydrogen-induced cracking, *Mater. Des.* 92 (2016) 300–305.
- [35] J. Kacher, I.M. Robertson, Quasi-four-dimensional analysis of dislocation interactions with grain boundaries in 304 stainless steel, *Acta Mater.* 60 (2012) 6657–6672.
- [36] S.L.I. Chan, H.L. Lee, J.R. Yang, Effect of retained austenite on the hydrogen content and effective diffusivity of martensitic structure, *Metall. Mater. Trans. A* 22 (1991) 2579–2586.
- [37] M. Wang, C.C. Tatan, M. Koyama, D. Ponge, D. Raabe, Enhancing hydrogen embrittlement resistance of lath martensite by introducing nano-films of interlath austenite, *Metall. Mater. Trans. A* 46 (2015) 3797–3802.